6-2021

Fabrication of Nd3+ and Yb3+ doped NIR emitting nano fluorescent probe: A candidate for bioimaging applications

D. Karthickraja

G. A. Kumar

D. K. Sardar

S. Karthi

Gamage C. Dannangoda
The University of Texas Rio Grande Valley

See next page for additional authors

Recommended Citation

Authors

D. Karthickraja, G. A. Kumar, D. K. Sardar, S. Karthi, Gamage C. Dannangoda, Karen S. Martirosyan, M. Prasath, M. Gowri, and E. L. Girija

Fabrication of Nd^{3+} and Yb^{3+} doped NIR emitting nano fluorescent probe: A candidate for bioimaging applications

D. Karthickraja [a], G.A. Kumar [b,c,d], D.K. Sardar [b], S. Karthi [e],
G.C. Dannangoda [f], K.S. Martirosyan [f], M. Prasath [g], M Gowri [a],
E.K. Girija [a]✻

[a] Department of Physics, Periyar University, Salem 636 011, Tamil Nadu, India.

[b] Department of Physics and Astronomy, University of Texas at San Antonio, San Antonio, Texas
78249, USA.

[c] Department of Atomic and Molecular Physics, Manipal University, Manipal 576 104, Karnataka,
India.

[d] Department of Natural Sciences, Texas agriculture and mechanical university, One University
Way, San Antonio, TX 78224, USA.

[e] College of Chemistry and Chemical Engineering, Henan University, Kaifeng 475004, PR China.

[f] Department of Physics and Astronomy, University of Texas at Rio Grande Valley, Brownsville,
Texas 78520, USA.

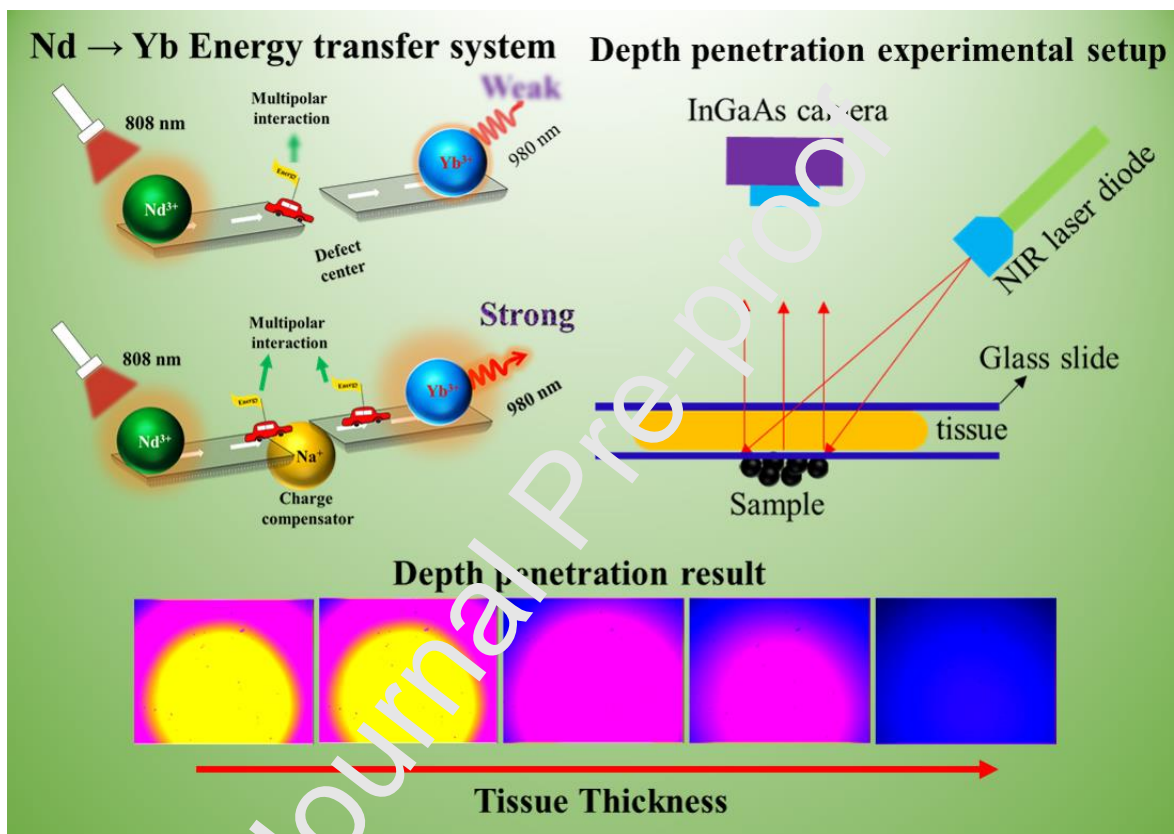[g] Department of Biotechnology, Bharathiar University, Coimbatore 641 046, Tamil Nadu India.

✻ **Corresponding author:**

Tel.: +91 9444391733

E-mail address:

girijaeaswaradas@gmail.com (E. K. Girija)

Graphical abstract

Abstract

The intentional design of rare earth doped luminescent architecture exhibits unique optical properties and it can be considered as a promising and potential probe for optical imaging applications. Calcium fluoride (CaF_2) nanoparticles doped with optimum concentration of Nd^{3+} and Yb^{3+} as sensitizer and activator, respectively, were synthesized by wet precipitation method and characterized by x-ray diffraction (XRD) and photoluminescence. In spite of the fact that the energy transfer takes place from Nd^{3+} to Yb^{3+}, the luminescence intensity was found to be weak due to the lattice defects generated from the doping of trivalent cations (Nd^{3+} and Yb^{3+}) for divalent host cations (Ca^{2+}). These defect centres were tailored *via* charge compensation approach by co-doping Na^+ ion and by optimizing its concentration and heat treatment duration. CaF_2 doped with 5 mol% Nd^{3+}, 3 mol% Yb^{3+} and 4 mol% Na^+ after heat treatment for 2 h exhibited significantly enhanced emission intensity and life time. The *ex vivo* fluorescence imaging experiment was done at various thickness of chicken breast tissue. The maximum theoretical depth penetration of the NIR light was calculated and the value is 14 mm. The fabricated phosphor can serve as contrast agent for deep tissue near infrared (NIR) light imaging.

Key words:

Calcium fluoride, Nanoparticle, Lanthanide, Energy transfer, Charge compensation, NIR imaging.

1. Introduction

Bioimaging is a modality for visualization of the tissues and organs of living beings noninvasively. Recently, optical imaging has gained immense interest because of nonionizing radiation, possibility for multimodal imaging with high sensitivity and resolution. Similarly a significant advancement in the field of nanotechnology has revolutionized the field of bioimaging leading to a transformation from conventional bioprobes to nanoprobes such as semiconductor quantum dots, rare earth doped nanoparticles *etc*. [1–3]. The trivalent rare earth ions doped luminescent nanocrystals have attracted considerable interest in diagnostic and therapeutic applications. Earlier much attention was paid for developing rare earth doped upconversion nanoparticles [4–7]. L. Lei *et al*., made several approaches to improve the upconversion luminescence intensity of Yb^{3+} /Er^{3+} doped core shell calcium fluoride (CaF_2) *via* co-doping sodium ion in the core, tuning Yb^{3+} concentration in shell and tailoring the shell thickness [8]. There are numerous studies on the development of upconversion luminescent nanoparticles for applications like optical imaging, photodynamic therapy (PDT), drug delivery and optogenetic stimulation [9–13]. Most of the upconversion nanoparticles were engineered with Yb^{3+} ion as a sensitizer due to its large absorption cross-section centering at 980 nm in the NIR region with a view to activate another rare earth ion such as Er^{3+}, Tm^{3+}, Ho^{3+} and Tb^{3+} thus resulting in anti-stokes shift process [14–16]. Since, visible light emitting upconversion luminescence generally involves multiphoton process, the quantum yield is usually lower than that of downconversion luminescence which considerably affects the efficacy of optical imaging during *in vitro* tracking and *in vivo* bio applications [12]. Moreover, one of the serious concerns with Yb^{3+} sensitized nanoparticle is that it induces local heating of

tissue when excited at 980 nm [15,17]. It is well documented that, upon irradiation with 980 nm laser the nanoparticles dissipates a lot of heat (~13 ºC) within 75 seconds. When compared to this, 808 nm laser irradiation has shown less heat dissipation (~7 ºC), that too for 300 seconds [18].

At present, the interest is shifted towards the development of rare earth doped NIR emitting downconversion nanoparticles due to their high photostability, long life time, less autofluorescence, good penetration depth in tissues, minimal photodamage and reduced scattering [19–21]. Such NIR emitting downconversion nanoparticles can be obtained by incorporating suitable rare earth ions in selected inorganic matrices. Thus, in comparison to Yb^{3+} based upconversion luminescence, Nd^{3+} based downconversion luminescence seems to be ideal for optical imaging applications as the absorption cross-section of Nd^{3+} at 800 nm is 10 times higher than that of absorption cross-section of Yb^{3+} at 980 nm [22,23]. Also Nd^{3+} provides both excitation and emission within the biological transparent windows. However, one of the caveats is that the emission spectrum of Nd^{3+} consists of four bands in the 900-1900 nm range with peak intensity at 1060 nm, so that the overall quantum yield of the emission is less at 1060 nm [24]. To avoid this, an activator that involves single photon relaxation by means of energy transfer process, can be introduced into the host matrix through co-doping. As Yb^{3+} has single excitation and emission electronic state ($^2F_{5/2}$ → $^2F_{7/2}$), it can be utilized as an activator to obtain high intense single emission at 980 nm [25].

Appropriate optical property and cytocompatibility of the bioprobes depends on choice of rare earth ion and host matrix. There are several host matrices used for rare earth doping such as $NaREF_4$ (RE^{3+} = Y^{3+}, Yb^{3+}, Gd^{3+} and Nd^{3+}) [12,14,15,26,27], LaF_3 [28], BaF_2 [29], GdF_3 [30], Y_2O_3 [31], fluorapatite [23,32,33] and hydroxyapatite [34,35]. Fluoride based host matrices gained attention because of their low phonon energy, tremendous optical transparency and high chemical stability even in harsh acidic condition. Among the fluoride host matrices CaF_2 is an excellent material with good

optical transparency between 0.13 μm – 10 μm and possesses a good biocompatibility [36,37]. Apart from this, the trivalent rare earth ion substitution in the divalent cation site leads to crystal lattice defects like cation site vacancies, local charge imbalance and rare earth ion cluster formation that would greatly quench the emission intensity, energy transfer efficiency and quantum yield. Co-doping of monovalent cation or anion along with rare earth ion is an usual strategy to compensate the local charge imbalance which also helps in reducing the lattice defects. The reduction of lattice defects in turn increases the energy transfer efficiency between sensitizer to activator, which substantially improve the quantum yield [8,16,38–41].

In this article, we report a systematic investigation on the synthesis and optimization of the heat treatment process of CaF_2 nanoparticle. The CaF_2 host nanoparticles are doped with rare earth ions such as Nd^{3+}/Yb^{3+} and simultaneously the emission property has been tuned by charge compensation via co-doping of sodium ion (Na^+). Apart from the synthesis, we have also performed the *ex vivo* experiments to study the penetration depth potential of emitted NIR signals from the phosphor.

2. Experimental procedure

2.1. Chemicals

Analytical grade calcium nitrate tetrahydrate [$Ca(NO_3)_2.4H_2O$, 98%], ammonium fluoride (NH_4F, 95%), sodium chloride [NaCl, 99.99%] and ammonia solution (NH_3, 25%) were obtained from Merck. Analar grade ytterbium nitrate pentahydrate [$Yb(NO_3)_3.5H_2O$, 99.9%] and neodymium nitrate hexahydrate [$Nd(NO_3)_3.6H_2O$, 99.9%] were procured from Sigma Aldrich. Double distilled water was employed as the solvent.

### 2.2. Synthesis of calcium fluoride nanoparticles

Pure CaF_2 nanoparticles were synthesized by wet precipitation method (Eqn. 1). Briefly, 2 M of ammonium fluoride solution was added dropwise into 1 M of calcium nitrate at 70 ºC by maintaining the pH of the solution at 7 with the addition of 25% ammonia solution. The appearance of white turbidity in the solution indicates the formation of CaF_2 nanocrystals. The obtained mixture was stirred for 30 minutes at 70 ºC and finally washed several times with double distilled water followed by drying at 80 ºC for 10 h. The resultant final product was heat treated at 600 ºC for 1 h and will be hereafter be referred as CF.

$$Ca^{2+} + 2F^- \rightarrow CaF_2 \qquad (1)$$
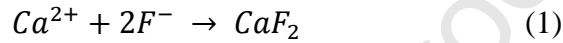
2.3. Synthesis of trivalent and monovalent ion substituted CaF_2 nanoparticles

2.3.1 Synthesis of Nd^{3+}/Yb^{3+} doped CaF_2 nanoparticles

Rare earth doped CaF_2 nanoparticles were synthesized following the same protocol mentioned above. Initially, the doping concentration of Yb^{3+} was set as 1 mol% and Nd^{3+} concentration was varied as 1, 2, 5, 8 and 10 mol%. Then as a second step, we fixed the Nd^{3+} concentration at 5 mol% and varied the Yb^{3+} concentration as 1.5, 3 and 6 mol%. The following chemical equation (Eqn.2) depicts the formation of trivalent rare earth ions doped CaF_2.

$$1 - (x + y)Ca^{2+} + xNd^{3+} + yYb^{3+} + 2F^- \rightarrow Ca_{1-(x+y)}Nd_xYb_yF_2 \qquad (2)$$
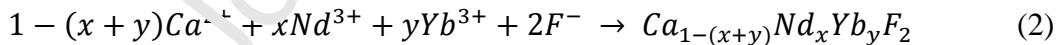
where, $y = 1$ mol% and $x = 1, 2, 5, 8$ and 10 mol% for Nd^{3+} optimization

$x = 5$ mol% and $y = 1.5, 3$ and 6 mol% for Yb^{3+} optimization

The resultant final product was heat treated at 600 ºC for 1 h and hereafter those samples will be referred as N1Y1, N2Y1, N5Y1, N8Y1, N10Y1, N5Y1.5, N5Y3 and N5Y6 respectively.

2.3.2. Synthesis of Na⁺ co-doped CaF$_2$:Nd^{3+}/Yb^{3+}(5 mol%/3 mol %) nanoparticles

Na$^+$ co-doped CaF$_2$:Nd^{3+}/Yb^{3+} nanocrystals were synthesized by adding appropriate (1, 4, 8, 12, 16 and 20 mol%) amount of NaCl solution into the calcium and rare earth nitrate solutions. This mixture was allowed to react with 2 M solution of ammonium fluoride to form Na$^+$ co-doped CaF$_2$:Nd^{3+}/Yb^{3+} nanocrystals. Finally, after washing the product it was heat treated at 600 ºC for 1 and 2 h and hereafter these samples will be referred as N5Y3S1-1h, N5Y3S4-1h, N5Y3S8-1h, N5Y3S12-1h, N5Y3S16-1h, N5Y3S20-1h, N5Y3S1-2h, N5Y3S4-2h, N5Y3S8-2h, N5Y3S12-2h, N5Y3S16-2h and N5Y3S20-2h. Equation 3 represents the formation of charge compensated CaF$_2$ nanocrystals.

$$1 - (x + y)Ca^{2+} + xNd^{3+} + yYb^{3+} + 2F^- + zNa^+ \rightarrow Ca_{1-(x+y)}Nd_xYb_yF_2:Na_Z \qquad (3)$$
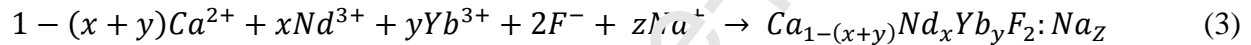
where, $x = 5$ mol%, $y = 3$ mol% and $z = 1, 4, 8, 12, 16$ and 20 mol %

3. Characterization

3.1. Phase, morphology and optical analysis

Phase purity of the as prepared samples was analyzed using Rigaku Miniflex II powder x-ray diffractometer (XRD) with Cu K-alpha source equipped with a Ni-filter for a monochromatic wavelength of 1.5406 Å. The XRD patterns of all samples were recorded in the 2θ range of 20-80º. The morphology, size and size distribution of the samples were observed and measured using scanning electron microscope (SEM, CARLZEISS EVO18) and high resolution transmission electron microscope (HRTEM, JEOL JEM-2100, Japan). The optical emission spectra of the rare earth doped CaF$_2$ samples were observed on excitation under 808 nm powered tunable fiber coupled Fabry Perot continuous laser diode (Thorlab, Model LM14S2) and the emission of the samples was recorded by the Quanta Master 51 spectrofluorimeter (Photon

Technology International Inc. NJ, U.S.) fitted with an InGaAs detector (Teledyne Judson Technologies, 062-8451, U.S.). The decay time measurement of $^4F_{3/2} \rightarrow {}^4I_{11/2}$ and $^2F_{5/2} \rightarrow {}^2F_{7/2}$ emission channels were recorded using Quantum Master 40 system with a single shot transient digitizer technique with a Nitrogen pumped Dye Laser (Photon Technology International part GL-3300 + GL-302) as excitation source. The Nitrogen laser, with 800 ps pulse width, pumps a high resolution dye chamber to give 488 nm light. The collected decay curve was analyzed using Origin 8 software (Origin lab, U.S.).

3.2. Cell culture and cytocompatibility assessment.

Fibroblast NIH 3T3 cells were cultured with 10% fetal bovine serum (FBS), 100 mg/ml penicillin and 100 U/ml streptomycin at 37 ºC under a humidified atmosphere of 5% CO_2 and 95% air. The cytotoxicity of samples CF and N5Y254 2h was examined with fibroblast NIH 3T3 cells using MTT (3-(4,5-dimethylthiazol-2-yl)-2,5-diphenyltetrazolium bromide tetrazolium) assay for an incubation period of 24 h. The procedure for conducting MTT assay was followed as per our previous report [42]. The cell viability was calculated using the expression,

$$Cell\ viability\ (\%) = \frac{OD_{Sample}}{OD_{Control}} \times 100 \qquad (4)$$

where, OD_{Sample} and $OD_{Control}$ are the optical densities of samples cultured with and without samples, respectively.

3.3. *Ex vivo* penetration depth experiment

Penetration depth experiment [43–45] was conducted using fresh chicken breast tissues purchased from the local supermarket. Tissue was sliced into different thickness such as 1.2, 1.9, 2.9, 3.5, 5.5, 7.5, 8.2, 10.3, 12.3 and 14.2 mm. A sliced tissue was sandwiched between two glass slides and introduced into microscope arrangement where the phosphor was placed below it.

808 nm NIR continuous laser diode (Axcel Photonics, MA, Power density 1.4 W/cm^2) was used

to excite the Nd^{3+} ions and the emitted luminescence signal was collected using InGaAs camera.

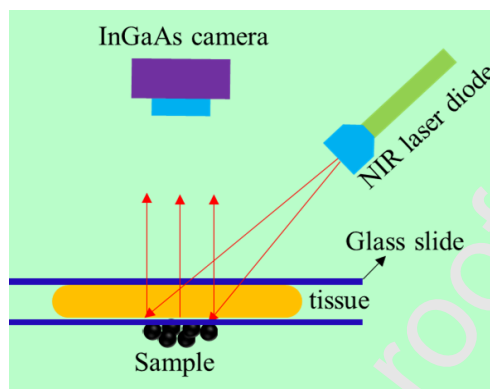Figure 1 depicts the schematic of *ex vivo* penetration depth analysis experimental arrangement [45].

Fig 1. Schematic representation of *ex vivo* penetration depth analysis experimental arrangement

4. Results

Figures 2*a* and 2*b* show the XRD patterns of the pure and different concentrations of

Nd^{3+} and Yb^{3+} doped samples. The XRD pattern of pure CaF$_2$ does not show any trace of

impurity and it matches well with the CPDS card for CaF$_2$ (35-0816) with cubic unit cell

structure [39]. The XRD patterns of the trivalent rare earth doped CaF$_2$ show wider diffraction

peaks which clearly reveals that the crystallite size and crystallinity decreased with the increase

in the dopant. When compared to pure CaF$_2$ the diffraction peaks of doped samples shifted

towards the lower angle side which confirms the incorporation of rare earth ions into the CaF$_2$

lattice site. The reason for the shift may be the slight mismatch of ionic radius (Ca^{2+} = 1 Å, Nd^{3+}

= 0.98 Å, Yb^{3+} = 0.99 Å) between calcium and rare earth ions that resulted in lattice expansion.

The cubic phase of the CaF$_2$ was formed to be stable even for higher doping concentration.

Figures 2*c* and 2*d* show that the XRD patterns of 1 and 2 h heat treated 1, 4, 8, 12, 16 and

20 mol% Na$^+$ co-doped N5Y3 samples respectively. It is interesting to note that even after

doping Na$^+$ ions along with rare earth ions, the CaF$_2$ nanoparticles retained its cubic phase and the observed peaks were found to match with the standard data. The very subtle deviations observed towards the low angle side indicates the lattice expansion. When compared to Na$^+$ free N5Y3 sample, the resolution and crystallinity have improved significantly after Na$^+$ co-doping and heat treatment.
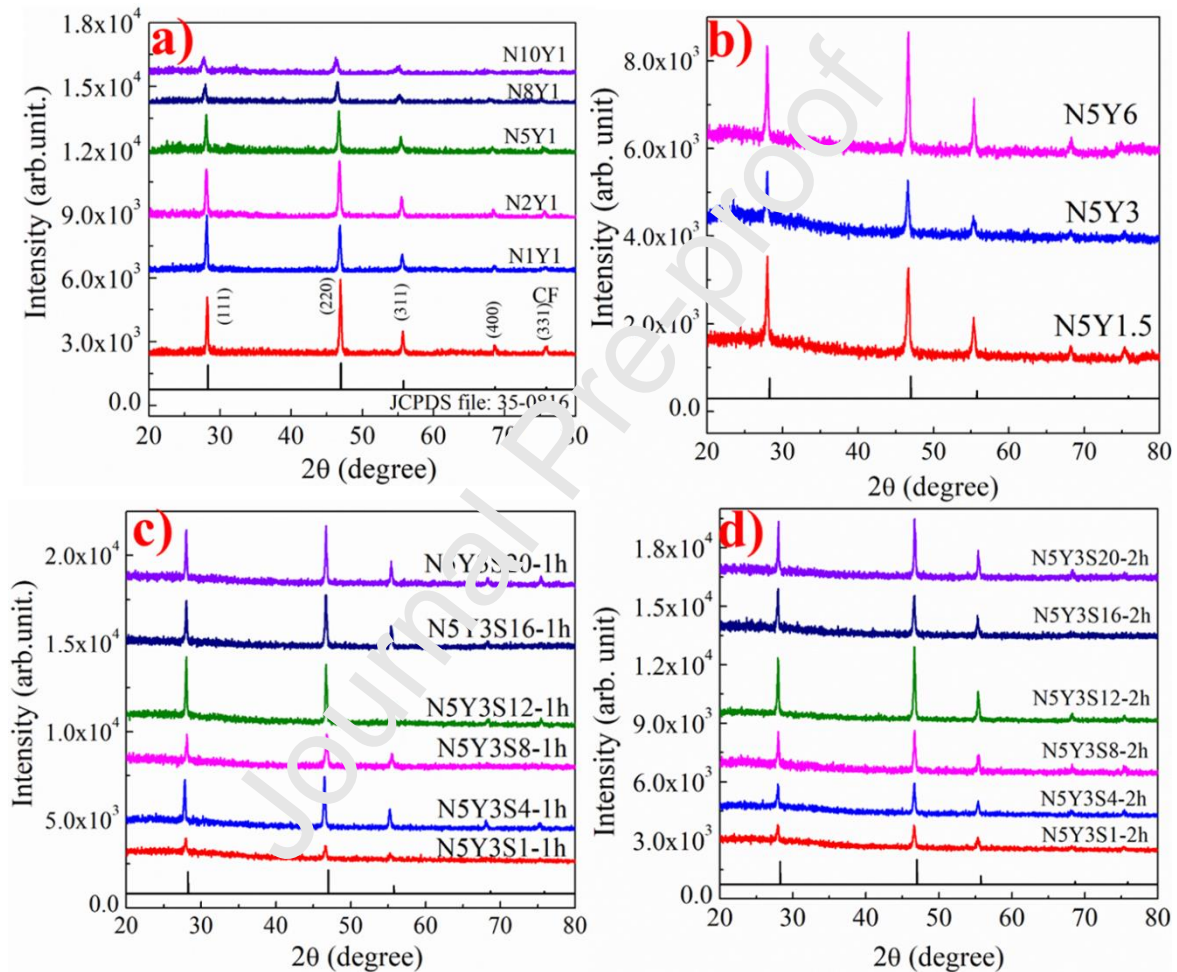

Fig 2. XRD patterns of *a&b*) pure & varying Nd^{3+} and Yb^{3+} doped 1 h heat treated CaF$_2$ and *c&d*) 1, 4, 8, 12, 16 and 20 mol% charge compensated N5Y3 sample with 1 & 2 h heat treatment.

Figure 3*a* shows the fluorescence spectra of samples with 1 mol% Yb^{3+} concentration *via* N1Y1, N2Y1, N5Y1, N8Y1 and N10Y1. Upon excitation under 808 nm all the samples exhibited emission at 980 nm which corresponds to the $^2F_{5/2} \rightarrow \, ^2F_{7/2}$ emission of Yb^{3+} ions [46]

and existence of intense emission at 980 nm in the emission spectrum dictates the Nd^{3+} to Yb^{3+} energy transfer in CaF_2 host. The emission intensity of the samples increased gradually with increase in concentration of Nd^{3+} ions up to 5 mol% and decreased beyond this concentration [Fig. 3b]. Indeed, the higher doping level of Nd^{3+} ion caused deleterious concentration quenching effect which effectively reduced the emission intensity of Yb^{3+}. Increase in Nd^{3+} concentration led to an increase of rare earth ion pair formation in the calcium fluoride lattice which effectively reduced the interionic distance between two Nd^{3+} ions when compared to Nd^{3+}-Yb^{3+} ions, thus favoring cross relaxation (CR) between Nd^{3+}-Nd^{3+} pairs [25,38].

Formation of pairs in CaF_2 lattice may be in the form sensitizer-sensitizer (Nd^{3+} - Nd^{3+}, named as A), activator-activator (Yb^{3+} - Yb^{3+}, named as B) and sensitizer-activator (Nd^{3+} - Yb^{3+}, named as C). Excited Nd^{3+} ions rapidly relax to ground state *via* energy transfer (ET), cross relaxation (CR) and energy migration (EM) [46,47]. Pair C would facilitate ET from $Nd^{3+} \rightarrow Yb^{3+}$ effectively through resonance overlapping between optical emission of sensitizer and absorption of activator. Pair A may help to EM but most of the case result in self quenching *via* cross relaxation ($^4F_{3/2}$, $^4I_{9/2} \rightarrow ^4I_{15/2}$). Figure 3$c$ represents the schematic illustration of possible transitions leading to ene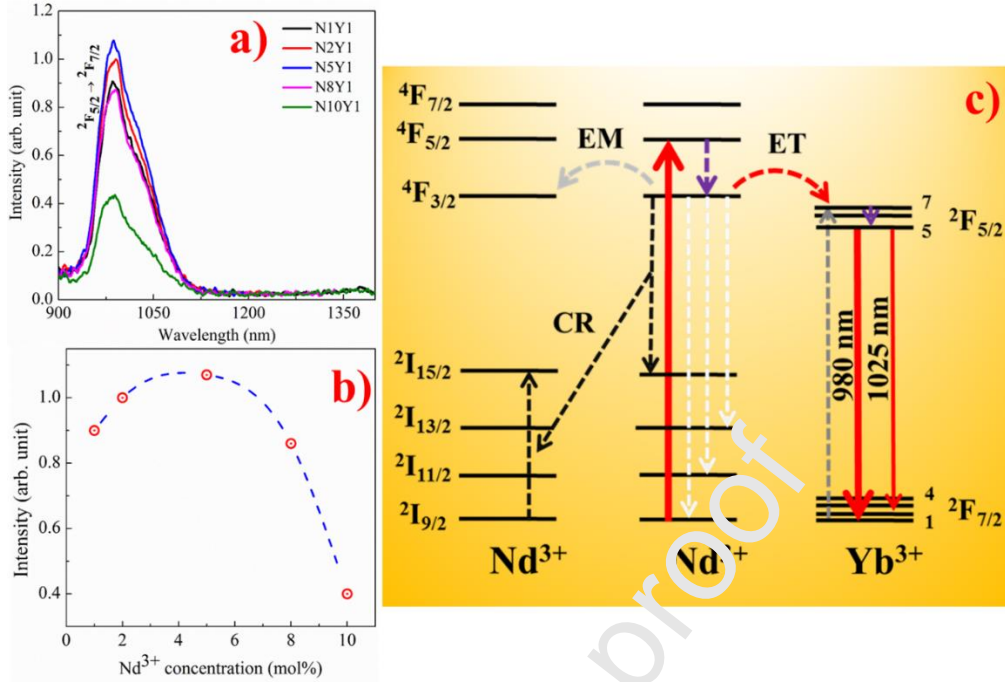rgy transfer, cross relaxation and energy migration from $Nd^{3+} \rightarrow Yb^{3+}$ and $Nd^{3+} \rightarrow Nd^{3+}$ pairs.

Fig 3. Emission spectra of *a*) **varying Nd^{3+} and fixed Yb^{3+} concentration,** *b*) **emission intensity as a function of Nd^{3+} for 980 nm ($^2F_{5/2} \rightarrow {}^2F_{7/2}$) emission and** *c*) **schematic illustration of Nd^{3+}-Yb^{3+} energy transfer system.**

It is obvious that the average distance (R_{DA}) between donor and acceptor plays an important role in the energy transfer from sensitizer to activator. R_{DA} was calculated using Blasse formula [48–50].

$$R_{DA} = 2\left(\frac{3V}{4\pi C_{x+y}Z}\right)^{\frac{1}{3}} \qquad (5)$$

where, V is the unit cell volume, C_{x+y} dopant concentration and Z (= 4) is the number of available cation site for dopant in the unit cell. Thus the estimated R_{DA} values are found to be 15.78, 13.85, 10.97, 9.66 and 9.03 Å for N1Y1, N2Y1, N5Y1, N8Y1 and N10Y1 respectively. N8Y1 and N10Y1 samples shows less R_{DA} (below 10 Å) when compared to other samples, which is due to the high concentration of Nd^{3+} ions forming more number of Nd^{3+} - Nd^{3+} pairs. In

this condition if the Nd^{3+} ions were excited at 808 nm, the excited energy may be transferred to the adjacent unexcited Nd^{3+} ions *via* EM and CR process which effectively quenches the emission intensity and thereby inhibiting the energy transfer efficiency from $Nd^{3+} \rightarrow Yb^{3+}$ ions.

Based on the above result, we fixed the Nd^{3+} concentration at 5 mol% and varied the Yb^{3+} concentrations up to 6 mol% and the corresponding emission spectra are shown in Fig. 4*a*. The emission (980 nm) intensity of the Yb^{3+} ion increased up to 3 mol% and then decreased rapidly due to concentration quenching [Fig. 4*b*]. A shoulder like emission is observed in the emission spectra centered around 1025 nm (marked with arrow). Phonon assisted energy migration from sensitizer to activator and crystal field splitting of Yb^{3+} ion may be responsible for the 1025 nm emission. $^2F_{5/2}(5) \rightarrow {}^2F_{7/2}(2)$ transition corresponds to 1025 nm and $^2F_{5/2}(5) \rightarrow {}^2F_{7/2}(1)$ transition is responsible for 980 nm emission and are shown in Fig. 3*c* [51]. When compared to N5Y1 sample the emission intensity increased ~7.75 fold for N5Y3 sample. The R_{DA} values of N5Y1.5, N5Y3 and N5Y6 are estimated to be 10.67, 9.98 and 9.01 Å, respectively.
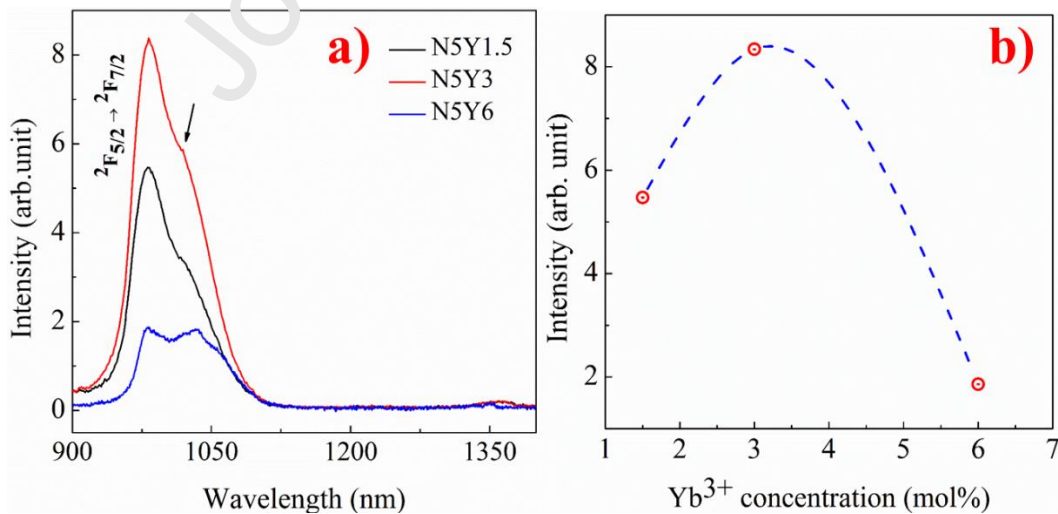
Fig 4. Emission spectra of *a*) varying Nd^{3+} and fixed Yb^{3+} concentration, *b*) emission intensity as a function of Yb^{3+} concentrations for 980 nm ($^2F_{5/2} \rightarrow {}^2F_{7/2}$) emission.

Figure 5*a* shows the emission spectra of 1 h heat treated N5Y3S1-1h, N5Y3S4-1h, N5Y3S8-1h, N5Y3S12-1h, N5Y3S16-1h and N5Y3S20-1h charge compensated (Na$^+$ = 1, 4, 8, 12, 16 and 20 mol%) samples. The 1 mol% sodium ion doped N5Y3S1-1h sample showed improved emission intensity (~1.25 fold) when compared to Na$^+$ free N5Y3 sample. While increasing the concentration of Na$^+$, the emission intensity got quenched more rapidly (Fig. 5*b*). One of the possible reasons for this rapid luminescence quenching could be associated with improper distribution of Na$^+$ ions in CaF$_2$ lattice at higher concentrations.

Figure 5*c* shows the emission spectra of charge compensated samples after 2 h heat treatment. Heat treatment for 2 h did not exhibit a linear enhancement of intensity with concentration. But when compared to 1 h heat treated samples, an enhancement in the emission intensity is observed for 2 h heat treated samples with 4 and 12 mol% Na$^+$ concentration. The observed enhancement in the emission intensity may be attributed to the proper distribution of Na$^+$ ions in CaF$_2$ lattice. When compared to N5Y3S1-1h sample the emission intensity has increased ~1.63 times for N5Y3S4-2h and N5Y3S12–2h sample. However, 1 mol% Na$^+$ co-doping may not be sufficient to compensate the defects entirely. 4 and 12 mol% Na$^+$ co-doped 2 h heat treated samples exhibit nearly equal emission intensity suggesting that 4 mol% may be the sufficient concentration for compensating the defects formed due to rare earth doping.

The energy transfer mechanism from sensitizer to activator can be understood from the Förster-Dexter theory. According to Förster-Dexter theory, overlapping between sensitizer emission and activator absorption bands may be responsible for the energy transfer process [46,52,53]. It has been reported that the quasi-resonant overlapping between Nd^{3+} emission at $^4F_{3/2}$/$^4I_{9/2}$ and Yb^{3+} absorption at $^2F_{7/2}$/$^2F_{5/2}$ favors the energy transfer from Nd^{3+} to Yb^{3+} *via*

exchange and multipolar interactions [54]. The exchange interaction is valid if average distance between Nd^{3+} and Yb^{3+} is less than 6 Å. In the present case, average distance between Nd^{3+} and Yb^{3+} was found to vary from approximately 9 to 16 Å. Hence, the multipolar interactions such as dipole-dipole, dipole-quadruple and quadruple-quadruple interactions may be accountable for energy transfer [48,51].
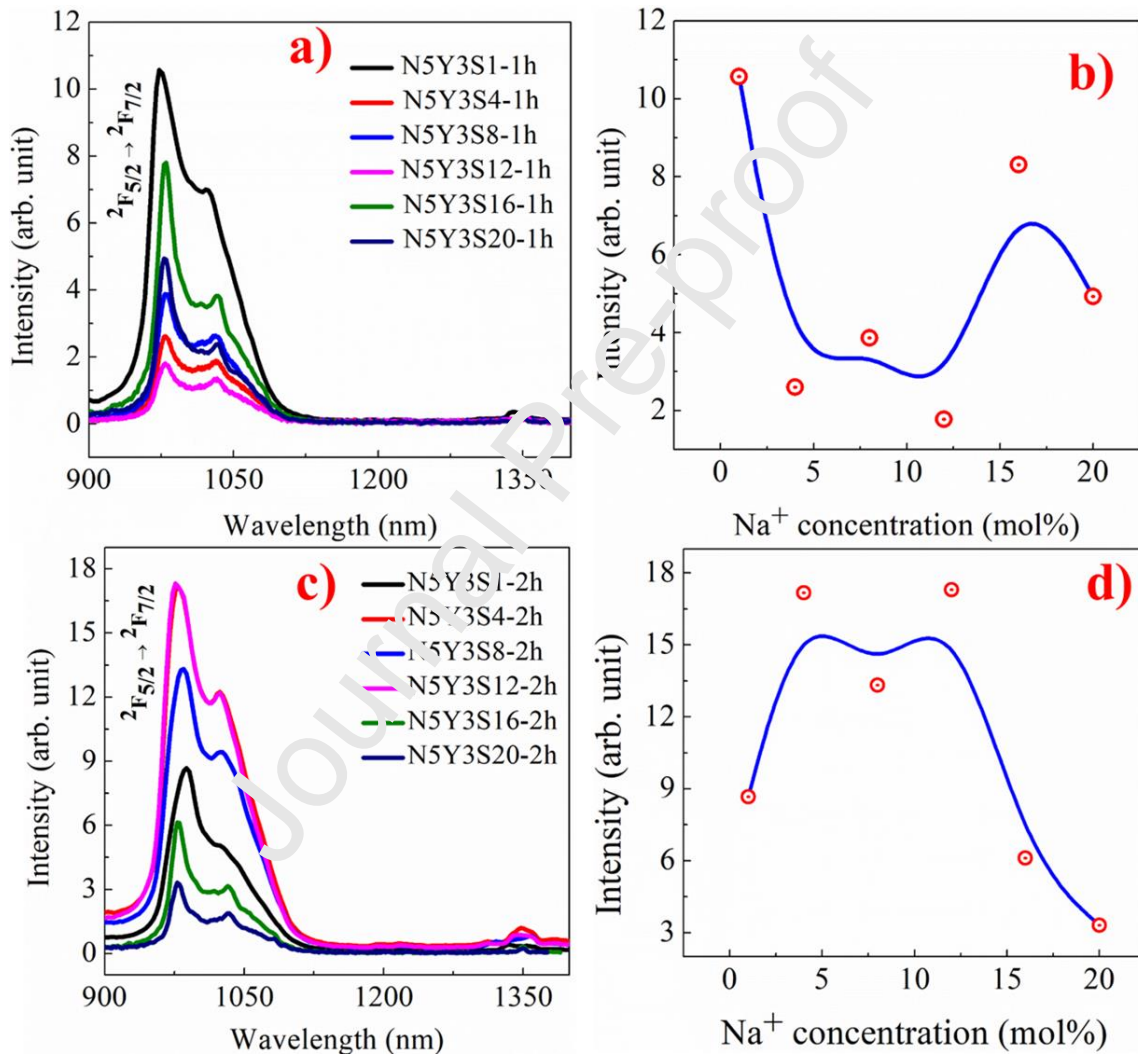

Fig 5. Emission spectra of *a&c*) 1 & 2 hrs heat treated 1, 4, 8, 12, 16 and 20 mol% charge compensated H5Y3 samples respectively and *b&d*) emission intensity as a function of Na$^+$ concentrations for 980 nm ($^2F_{5/2} \rightarrow {}^2F_{7/2}$) emission with 1 & 2 h heat treatment.

The decay kinetics of the selected samples have been investigated using bi-exponential expression followed by calculation of average life time of phosphors using the Eqn. 6 and 7 [23,24,55].

$$I(t) = A_1 \exp\left(-\frac{t}{\tau}\right) + A_2 \exp\left(-\frac{t}{\tau}\right) \tag{6}$$

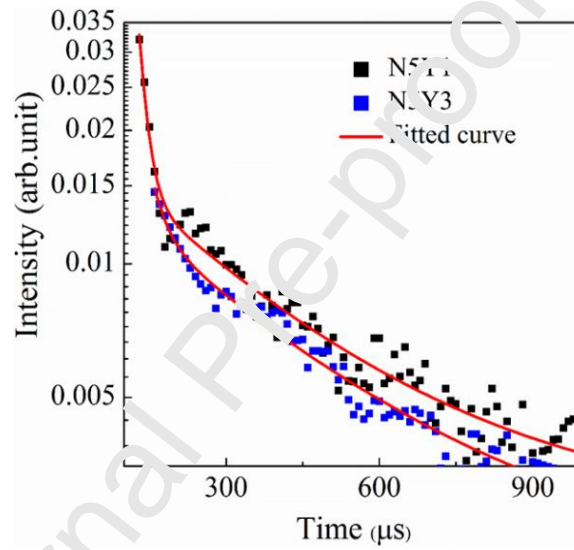$$\tau_{av} = \frac{A_1 \tau_1^2 + A_2 \tau_2^2}{A_1 \tau_1 + A_2 \tau_2} \tag{7}$$

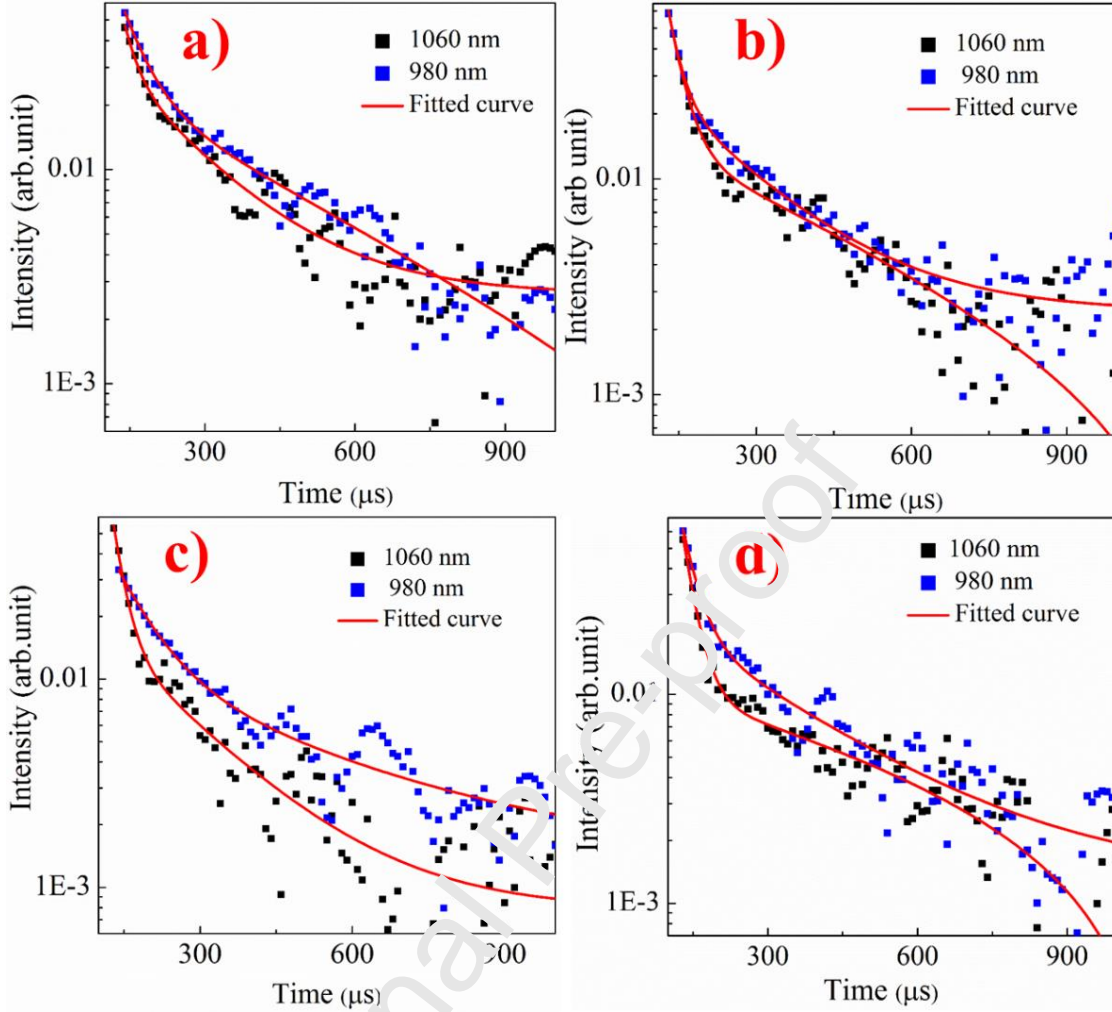**Fig 6. Decay curves of $^2F_{5/2} \rightarrow {}^2F_{7/2}$ emission channel for N5Y1 and N5Y3 samples.**

Fig 7. Decay curves of *a*) N5Y3S1-1h, *b*) N5Y3S1-2h, *c*) N5Y3S4-2h and *d*) N5Y3S12-2h **samples for** $^4F_{3/2} \rightarrow {}^4I_{11/2}$ **and** $^2F_{5/2} \rightarrow {}^2F_{7/2}$ **emission channels.**

where A_1 and A_2 are the fitting parameters and τ_1 and τ_2 are the mean life time. The decay time corresponding to the $^2F_{5/2} \rightarrow {}^2F_{7/2}$ emission channel of Yb^{3+} was measured for N5Y1 and N5Y3 samples which resulted in a mean life time of 19.2 and 78.1 µs, respectively, as per the fitting shown in Fig 6. It is obvious that, when increasing the Yb^{3+} concentration the decay time at 980 nm is increased. This may be attributed to the reduction of the average distance between Nd^{3+} and Yb^{3+}, which resulted in efficient energy transfer.

Figures 7*a* and 7*b* show that the fitted decay time data for 1060 nm and 980 nm of 1 mol% charge compensated 1 and 2 h heat treated N5Y3 samples. After 1 mol% charge

compensation the life time of N5Y3 sample at $^2F_{5/2} \rightarrow {}^2F_{7/2}$ transition increases by 1.64 fold

when compared to Na^+ free N5Y3 sample. The same sample when heat treated for 2 h showed

decreased life time for $^2F_{5/2} \rightarrow {}^2F_{7/2}$ transition (~2.8 fold) and increased life time for $^4F_{3/2} \rightarrow {}^4I_{11/2}$

transition (~2.44 fold). These results suggest that 1 mol% Na^+ doping may not compensate the

defects entirely.

Figure 7c shows the experimental (solid square pattern) and fitted decay time (solid line)

for N5Y3S4-2h sample at 1060 nm and 980 nm. Indeed, when increasing the co-doping of Na^+ to

4 mol%, the life time of $^2F_{5/2} \rightarrow {}^2F_{7/2}$ transition increased to ~2.31 fold while the life time of

$^4F_{3/2} \rightarrow {}^4I_{11/2}$ decreased to ~3.44 fold that of the N5Y3S1-2h sample which suggest that the

efficient energy transfer may be taking place in the N5Y3S4-2h sample. The 12 mol% Na^+ co-

doped sample shows relatively shorter life time when compared to 4 mol% Na^+ co-doped sample

[Fig 7d and Table 1]. The values of fitting parameters and calculated average life time for $^4F_{3/2}$

$\rightarrow {}^4I_{11/2}$ and $^2F_{5/2} \rightarrow {}^2F_{7/2}$ emission channels are listed in Table 1.

Table 1. Average life time and fitting parameters for $^4F_{3/2} \rightarrow {}^4I_{11/2}$ and $^2F_{5/2} \rightarrow {}^2F_{7/2}$ emission channels of Nd^{3+} and Yb^{3+} respectively.

Emission Channel	Sample code	A_1	τ_1 (μs)	A_2	τ_2 (μs)	τ_{av} (μs)
$^4F_{3/2} \rightarrow {}^4I_{11/2}$	N5Y3S1-1h	0.055	164.144	5.047	25.435	34.7
	N5Y3S1-2h	0.017	900.618	8.402	25.053	84.8
	N5Y3S4-1h	14.172	22.159	2.86E-02	175.955	24.6
	N5Y3S12-1h	0.020	406.374	5.084	27.695	48.5
$^2F_{5/2} \rightarrow {}^2F_{7/2}$	N5Y1	0.016	350.181	45.391	16.676	19.2
	N5Y3	0.014	376.126	1.150	27.489	78.1
	N5Y3S1-1h	0.646	47.211	0.032	347.060	128
	N5Y3S1-2h	0.029	259.767	3.454	29.549	45.6
	N5Y3S4-2h	0.169	68.561	1.48E-02	341.269	151

N5Y3S12-2h	10.045	23.126	0.043	117.373	25.1

Figure 8*a* shows the SEM image of pure CF nanoparticles which are spherical in shape. Due to aggregation of the particles it was difficult to estimate the size. Figure 8*b* shows the TEM photograph of the CF sample which clearly reveals the nearly spherical like morphology agreeing well with the SEM observation. The average particle size of CF sample was found to be 110 ± 40 nm. The inset at bottom right in Fig. 8*b* clearly reveals the spherical morphology of CF. The selected area electron diffraction (SAED) pattern revealed bright spots along with concentric rings indicating the polycrystalline nature of the nanoparticles (inset at top right in Fig 8*b*). Figure 8*c* shows the histogram plot of particle size distribution along with Gaussian distribution obtained from TEM image using Image analysis program imageJ software.
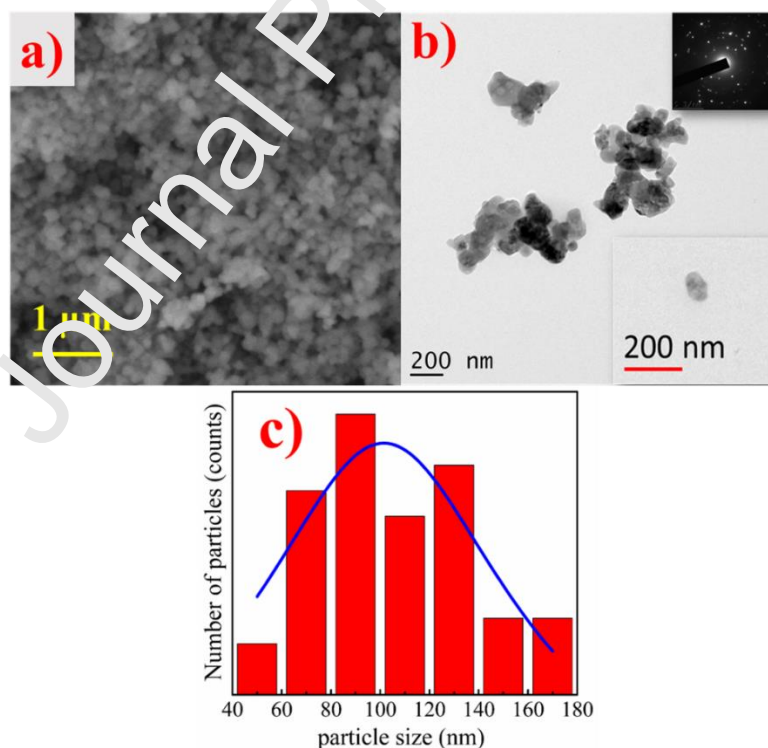

Fig 8. Morphological analysis of pure calcium fluoride *a*) SEM image, *b*) TEM image (the top inset shows the SAED pattern and the bottom image revealed the spherical shape of the particle) and *c*) Particle size distribution.
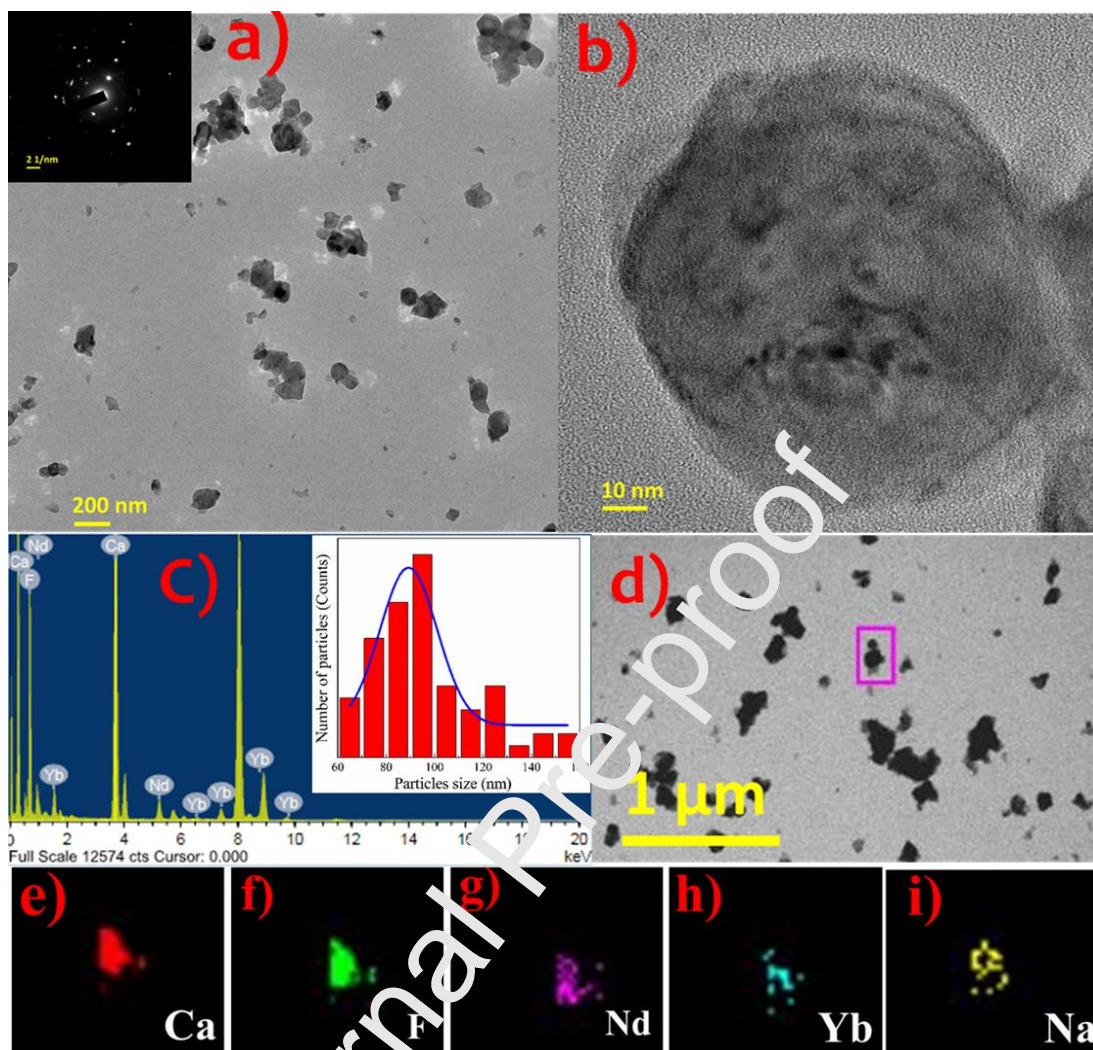
Fig 9. Morphology and elemental analysis of N5Y3S4-2h sample *a&b*) TEM images, *c*) EDS spectra and *d-i*) TEM image and elemental mapping. (Inset at top left in fig 9*a* and inset at right in fig 9*c* are the SAED pattern and particle size distribution, respectively)

Figures 9 (*a*) and (*b*) show the TEM images of the N5Y3S4-2h sample. The particles were found to be aggregated and spherical in morphology. The average particle size was found to be 110 ± 30 nm and which is almost same as that of undoped CF sample. The inset in Fig. 9 (*a*) is the SAED pattern, the bright spots are arranged in repeated regular order which clearly indicates the improvement of crystallinity after doping when compared the SAED pattern of sample CF. Figures 9 (*c-i*) are the energy dispersive x-ray spectra (EDS) and TEM image along with corresponding elemental mapping images of the N5Y3S4-2h sample. EDS confirmed presence of

elements such as Ca, F, Nd, Yb and Na and the mapping study confirms the distribution of the doped elements in throughout the host matrix. The right inset in Fig 9 (*c*) shows the particle size distribution along with Gaussian fit.
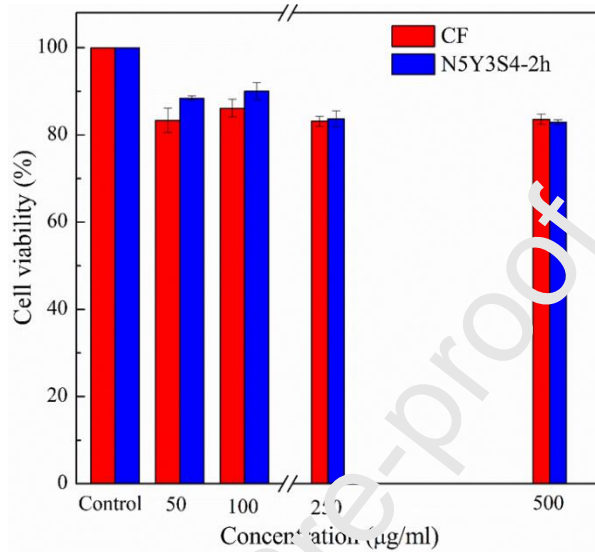

Fig 10. Cytocompatibility of the CF and N5Y3S4-2h samples with NIH 3T3 cells.

Figure 10 shows the cytocompatibility assessments of samples CF and N5Y3S4-2h which was examined using fibroblast NIH 3T3 cells with different dosage *viz* 0, 50, 100, 250 and 500 µg/ml. When compared to control the cells treated with sample showed less cell viability. It can be observed that when increasing dosage of the samples showed almost same viability of about more than 83% and even after incubating higher concentration up to 500 µg/ml. According to the biological evaluation of medical devices-part 5: tests for in vitro cytotoxicity (ISO 10993-5:2009), if the viability of the cell in presence of the material is less than 70% then the material is considered to be cytotoxic [56]. Above experiment clearly reveals that samples are cytocompatible.
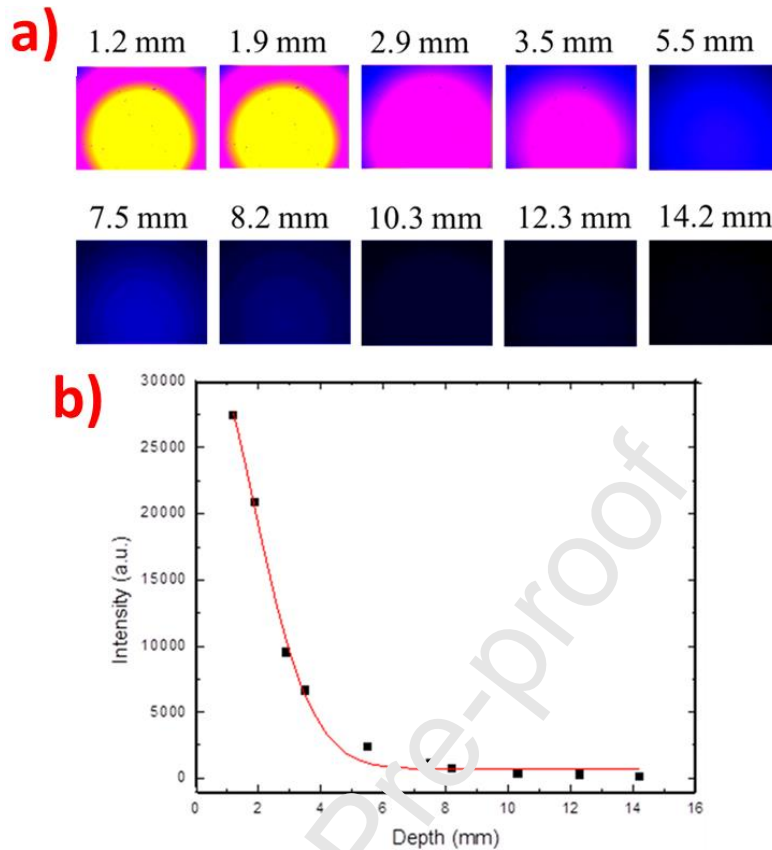
Fig 11. Penetration depth measurement of N5Y3S4-2h nanoparticles with chicken breast tissue, *a*) fluorescence for different tissue thickness and *b*) florescence intensity vs depth profile along with exponential decay fit.

In order to explore the deep tissue NIR imaging capability of N5Y3S4-2h nanoparticles, the penetration depth measurement experiment was conducted using chicken breast tissue. Figure 11 (*a*) shows the fluorescence observed for different tissue thickness. It is found that the fluorescence intensity is high for tissue thickness up to 1.9 mm. With increasing the tissue thickness the fluorescence intensity decreased and was detectable up to 8.2 mm. The maximum depth penetration of the NIR signals was assessed by fitting the experimental fluorescence intensity *vs* depth (thickness) of the tissue using exponential decay function as shown in Fig. 11(b). From the fitting, maximum theoretical depth penetration of the NIR light was estimated as 14 mm.

5. Discussion

Bioimaging is a versatile imaging technique that helps to understand the structure of biological tissues and their functions. Among the variety of imaging techniques, optical imaging is a unique technique that possesses a resolution to the cellular level using light as the optical tool. Recently, rare earth doped NIR emitting nanoparticles have attracted much attention due to the advantages over the limitations of other conventional bioprobes. Penetration depth of NIR light in tissues directly relates to the emission intensity and hence, it is necessary to develop intense NIR emitting small particles. Herein, we adopted a trustworthy and simple approach to tune the emission intensity *via* Na^+ ion co-doping along with rare earth ions.
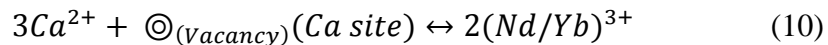
Pristine rare earth and sodium co-doped CaF_2 nanocrystals were synthesized by facile wet precipitation method with systematic investigations on dopant concentrations. Initially the doping level of Yb^{3+} ion was kept fixed and Nd^{3+} was varied to optimize Nd^{3+} concentration. Based on the down conversion luminescence spectra of the samples obtained concentration of Nd^{3+} was fixed at 5 mol% and then the concentration of Yb^{3+} was varied up to 6 mol% and optimized the Yb^{3+} concentration as 3 mol%. Finally, 5 mol% and 3 mol% of Nd^{3+} and Yb^{3+}, respectively, doped sample was chosen for further experiments.

The phase purity of the rare earth doped sample was confirmed by XRD, even at higher doping of rare earth ions, the CaF_2 host retained its cubic structure and did not show any other optical active or optical inactive phase formation. Nd^{3+} alone doped 1 h heat treated sample has showed 1060 nm relaxation under 808 nm excitation (Fig. S1). In order to exploit the whole excited energy one more rare earth ion Yb^{3+} was introduced which favored the single photon relaxation yielding the single and broad emission centered at 980 nm clearly revealing the energy
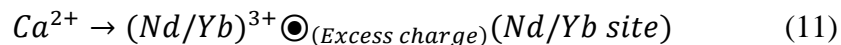
transfer that has taken place from $Nd^{3+} \rightarrow Yb^{3+}$. The quasi-resonance overlapping of Nd^{3+} emission and Yb^{3+} absorption bands helped the energy transfer from $Nd^{3+} \rightarrow Yb^{3+}$ *via* multipolar interaction. The life time of N5Y3 sample at 980 nm emission was found to be 78.1 μs. Figure 12 (*a*) represents the schematic illustration of possible energy transfer process from $Nd^{3+} \rightarrow Yb^{3+}$ in CaF_2 nanoparticle. Here, less intense and weak emission may be attributed to the cross-relaxation between the sensitizer to sensitizer and lattice defects formed in the host.

To investigate such weak luminescence, we examined the formation of structural disorders and defects after rare earth doping in the host matrix. When trivalent rare earth ions were introduced into the CaF_2 crystal lattice, creation of lattice defects site vacancies and lattice distortion as means of local charge balance mechanism is unavoidable. Figures S2 (*a*), (*b*) and (*c*) show the schematic illustration of pure and rare earth doped calcium fluoride lattice. CaF_2 crystalizes in a cubic unit cell structure where fluorine ion occupies corners of the cubes and calcium ions occupies center of every other eight fold coordinate site. Equation 10 reveals the possible cation vacancies creation mechanism after rare earth ion doping. There are two rare earth ions occupying three calcium sites, hence to maintain charge neutrality one calcium site vacancy is created. Another possibility is each trivalent cation substituted in divalent cation site creates excess charge in trivalent site [Eqn. 11]. In order to eliminate the charge imbalance and site vacancies, monovalent cation or anion were additionally introduced into the system with a view to reduce possible defects formation in crystal lattice [8, 40, 41].

1. Vacancy formation

$$3Ca^{2+} + \odot_{(Vacancy)}(Ca\ site) \leftrightarrow 2(Nd/Yb)^{3+} \qquad (10)$$

2. Local charge imbalance

$$Ca^{2+} \rightarrow (Nd/Yb)^{3+} \odot_{(Excess\ charge)}(Nd/Yb\ site) \qquad (11)$$

It is necessary to compensate the local charge in the rare earth doped calcium fluoride crystal lattice by considering charge compensation mechanism for refining the luminescent property of such nanoparticles. Here, we used monovalent Na^+ ion as a charge compensator, which was co-doped with the CaF_2:Nd^{3+}/Yb^{3+} system. Co-doping of Na^+ ion was done with sodium to rare earth ratio of 1:8, 4:8, 8:8, 12:8, 16:8, and 20:8 mol%. Sodium ion may occupy the vacancy site in CaF_2 lattice and eliminate the calcium site vacancy and local charge imbalance [Fig. S2 (*d*)]. The combination of rare earth and sodium ions replaced by two calcium site maintains the charge neutrality (refer Eqn. 12).

$$2Ca^{2+} \leftrightarrow (Nd/Yb)^{3+} + Na^+ \qquad (12)$$
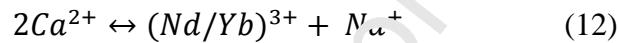
Interestingly, our studies revealed that after co-doping of sodium ions into the CaF_2:Nd^{3+}/Yb^{3+} the emission intensity enhanced significantly, since, co-doped Na^+ ions may compensate the defects formed due to charge imbalance and thereby reduce optical quenching. 1 mol% Na^+ co-doped sample showed enhanced intensity for 1 h heat treatment while the other samples exhibited comparatively less intensity. Whereas on 2 h heat treatment, 4 and 12 mol% Na^+ co-doped samples revealed almost similar intensity which is much more higher than 1 hour heat treated 1 mol% Na^+ co-doped sample. As far as the life time is concerned, 4 mol% Na^+ co-doped sample exhibits higher life time then Na^+ free N5Y3, N5Y3S1-1h and N5Y3S12-2h sample. Hence, 4 mol% Na^+ co-doped N5Y3 sample is considered to be the potential candidate for bioprobing applications.

Figure 12 (*b*) shows the schematic illustration of energy transfer process from $Nd^{3+} \rightarrow Yb^{3+}$ after charge compensation *via* Na^+ doping in calcium fluoride nanoparticles. Here, the defect centers which are the energy quenching centres were repaired by the Na^+ ions that enabled the enhancement of emission intensity in CaF_2: Nd^{3+},Yb^{3+} specimen by reducing the

defects. There was a strong energy transfer from $Nd^{3+} \rightarrow Yb^{3+}$ that resulted in intense near infrared emission at 980 nm. Affirming of optical imaging capability of the charge compensated phosphor was investigated by *ex vivo* depth penetration experiment with different chicken breast tissue thicknesses. The expected decrease of fluorescence intensity with increase in tissue thickness was observed and the maximum depth penetration capability of the NIR light were calculated and the value was found to be 14 mm. From this experiment we have confirmed that the fabricated phosphor have a potential for analyzing the deep tissues.
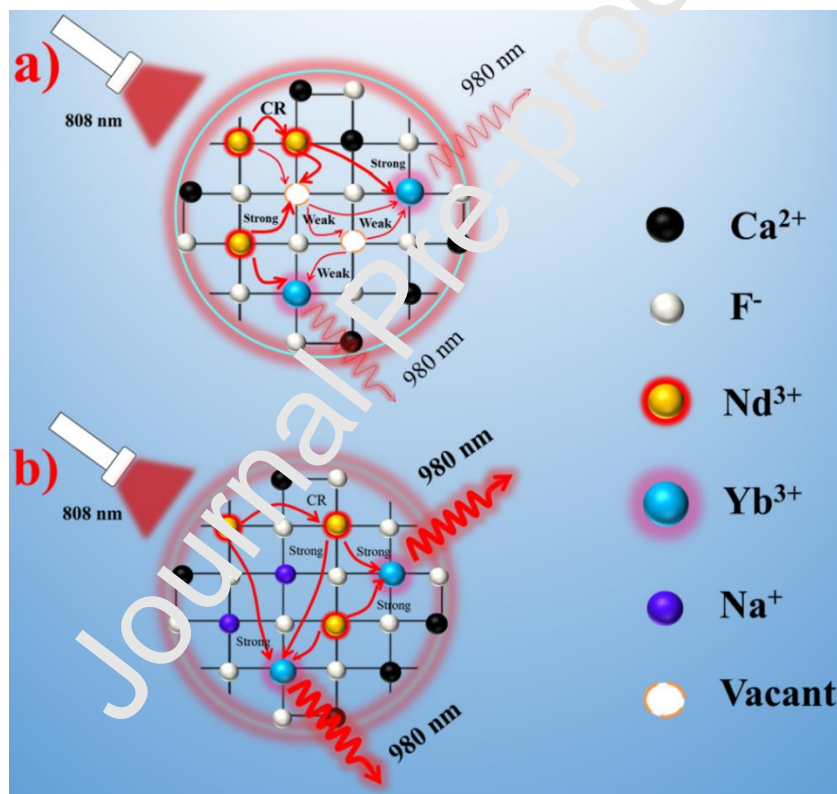

Fig 12. Schematic illustration of $Nd^{3+} \rightarrow Yb^{3+}$ energy transfer in CaF_2 a) before and b) after charge compensation.

6. Conclusion

We have successfully tuned the optical properties of Nd^{3+} and Yb^{3+} doped calcium fluoride luminescent particles *via* co-doping of Na^+ ions and heat treatment. All the luminescent specimens exhibit intense near infrared emission at 980 nm when excited at 808 nm laser, thereby suggesting the energy transfer from $Nd^{3+} \rightarrow Yb^{3+}$. After co-doping of Na^+ ion in $CaF_2:Nd^{3+}/Yb^{3+}$ lattice the emission intensity increased significantly. Hence, 4 mol% Na^+ co-doped $CaF_2:Nd^{3+}/Yb^{3+}$ considered as the potential bioprobe for optical imaging applications. The *ex vivo* depth penetration experiment clearly dictates prepared phosphor's potential to act as contrast agent for deep tissue optical imaging applications. The developed luminescent probe shows promising *ex vivo* depth penetration, which may be developed as a single nano probe with multifunctional performance for theranostic applications in future.

Highlights

- ➤ We have successfully prepared the $Nd^{3+} \rightarrow Yb^{3+}$ energy transfer system.
- ➤ Defects in $CaF_2:Nd^{3+}/Yb^{3+}$ lattice are repaired with Na^+ ion co-doping
- ➤ The optical property of luminescent particles have been tuned *via* co-doping of Na^+ and heat treatment process.
- ➤ *Ex vivo* optical imaging experiment confirms the feasibility of deep tissue imaging

Acknowledgement

demise of Dr. S. Karthi on 7th August 2020, who was actively involved with this work, data analysis and in the initial stages of manuscript preparation

Conflicts of interest

There are no conflicts to declare

Reference

1   D. Kim, N. Lee, Y. Il Park and T. Hyeon, *Bioconjug. Chem.* 2017, **28**, 115–123. https://doi.org/10.1021/acs.bioconjchem.6b00654.

2   R. Wang and F. Zhang, *J. Mater. Chem. B*, 2014, **2**, 2422–2443. https://doi.org/10.1039/c3tb21447h.

3   B. R. Smith and S. S. Gambhir, *Chem. Rev.*, 2017, **117**, 901–986. https://doi.org/10.1021/acs.chemrev.6b00073.

4   J. Yu, Y. Rong, C. Kuo, X. Zhou and D. T. Chiu, *Anal. Chem*, 2017, *89*, 42-56. https://doi.org/10.1021/acs.analchem.6b04672.

5   J. W. Chung, Z. Gerelkhuu, J. H. Oh and Y. I. Lee, *Appl. Spectrosc. Rev.*, 2016, **51**, 678–705. https://doi.org/10.1090/05704928.2016.1167070

6   S. Wen, J. Zhou, K. Zheng, A. Bednarkiewicz, X. Liu and D. Jin, *Nat. Commun.*, 2018, **9**, 1-12. https://doi.org/10.1038/s41467-018-04813-5.

7   H. Dong, S. Du, X. Zheng, G. Lyu, L. Sun, L. Li, P. Zhang, C. Zhang and C. Yan, *Chem. Rev,* 2015, *115*, 10725-10815. https://doi.org/10.1021/acs.chemrev.5b00091..

8   L. Lei, B. Xie, Y. Li, J. Zhang and S. Xu, *J. Lumin.*, 2017, **190**, 462–467. https://doi.org/10.1016/j.jlumin.2017.05.084.

9   C. Shell, S. Upconversion, J. He, M. Liu, F. Wang and P. Shi, *Nano Letters*, 2018, **18**, 948-956. https://doi.org/10.1021/acs.nanolett.7b04339.

10   M. Buchner, P. García Calavia, V. Muhr, A. Kröninger, A. J. Baeumner, T. Hirsch, D. A. Russell and M. J. Marín, *Photochem. Photobiol. Sci.*, 2019, **18**, 98–109.

https://doi.org/10.1039/c8pp00354h.

11   L. L. Fedoryshin, A. J. Tavares, E. Petryayeva, S. Doughan and U. J. Krull, *ACS Appl. Mater. Interfaces*, 2014, **6**, 13600–13606. https://doi.org/10.1021/am503039f

12   G. Chen, Y.O. Tymish, L. Sha, L. Wing-Cheung, W. Fang, T.S. Mark, A. Hans, N.P. Paras, *ACS nano*, 2012, **6**, 2969-2977. https://doi.org/10.1021/nn2042362.

13   F. Ai, Q. Ju, X. Zhang, X. Chen, F. Wang and G. Zhu, *Sci. Rep.*, 2015, **5**, 1–11. https://doi.org/10.1038/srep10785.

14   J. A. Damasco, G. Chen, W. Shao, H. Ågren, H. Huang, W. Song, J. F. Lovell and P. N. Prasad, *ACS Appl. Mater. Interfaces*, 2014, **6**, 13884–13893. https://doi.org/10.1021/am503288d.

15   Q. Zhan, Q. Jun, L. Huijuan, S. Gabriel, W. Dan, H. Sailing, Z. Zhiguo, A.E. Stefan. *ACS nano,* 2011, **5**, 3744-3757. https://doi.org/10.1021/nn200110j.

16   L. Lyu, H. Cheong, X. Ai, J. Lin and B. Xing, *NPG Asia Mater.*, 2018, 685–702. https://doi.org/10.1038/s41427-018-0065-y.

17   Y. Wang, G. Liu, L. Sun, J. Xiao, J. Zhou, C. Yan and W. E. T. Al, *ACS nano*, 2013, **7**, 7200-7206. https://doi.org/10.1021/nn402601d.

18   X. Chen, Y. Tang, A. Liu, Y. Zhu, D. Gao, Y. Yang, J. Sun, H. Fan and X. Zhang, *ACS Appl. Mater. Interfaces*, 2018, **10**, 14378–14388. https://doi.org/10.1021/acsami.8b00409.

19   J. Xu, L. Xu, C. Wang, R. Yang, Q. Zhuang, X. Han, Z. Dong, W. Zhu, R. Peng and Z. Liu, *ACS nano*, 2017, **11**, 4463-4474. https://doi.org/10.1021/acsnano.7b00715.

20   B. Xu, X. Zhang, W. Huang, Y. Yang, Y. Ma, Z. Gu, T. Zhai and Y. Zhao, *J. Mater. Chem. B*, 2016, **4**, 2776–2784. https://doi.org/10.1039/c6tb00542j.

21   X. Li, W. Rui, Z. Fan, Z. Lei, S. Dengke, Y. Chi, Z. Dongyuan, *Sci. Rep.* 2013, **3**, 3536. https://doi.org/10.1038/srep03536.22

22   Q. Shao, Z. Yang, G. Zhang, Y. Hu, Y. Dong and J. Jiang, *ACS Omega*, 2018, **3**, 188–197. https://doi.org/10.1021/acsomega.7b01581.

23   S. Karthi, G. A. Kumar, D. K. Sardar, C. Santhosh and E. K. Girija, *Opt. Mater,* 2018, **77**, 39–47. https://doi.org/10.1016/j.optmat.2018.01.013.

24   L. C. Mimun, G. Ajithkumar, C. Rightsell, B. W. Langloss, M. J. Therien and D. K. Sardar, *J. Alloys Compd.*, 2017, **695**, 280–285. https://doi.org/10.1016/j.jallcom.2016.10.202.

25   C. Cao, M. Xue, X. Zhu, P. Yang, W. Feng and F. Li, *ACS Appl. Mater. Interfaces,* 2017, **9**, 18540-18548. https://doi.org/10.1021/acsami.7b04305.

26   R. Kumar, M. Nyk, T. Y. Ohulchanskyy, C. A. Flask and P. N. Prasad, *Adv. Funct. Mater.*, 2009, **19**, 853–859. https://doi.org/10.1002/adfm.200800765.

27   F.J. Pedraza, R. Chris, G.A. Kumar, G. Jason, M. Carlos, K.S. Dhiraj, K.S, *Appl. Phys. Lett*. 2017, **110**, 223-107. https://doi.org/10.1063/1.4984140.

28   U. Rocha, K. U. Kumar, C. Jacinto, I. Villa, F. Sanz-rodríguez, C. Iglesias, D. Cruz, A. Juarranz, E. Carrasco, F. C. J. M. Van Veggel and E. Bovero, *Small.* 2014, **10**, 1141-1154. https://doi.org/10.1002/smll.201301716.

29   R. K. Sharma, S. Nigam and Y. N. Chouryal, *ACS Appl. Nano Mater,* 2019, **2**, 927-936. https://doi.org/10.1021/acsanm.8b02180.

30   V. A. Online, M. Pokhrel, L. C. Mimun, B. Yust, G. A. Kumar, A. Dhanale, L. Tang and D. K. Sardar, *Nanoscale,* 2014, **6**, 1667–1674. https://doi.org/10.1039/c3nr03317a.

31   A. Lupei, V. Lupei, A. Ikesue, C. Gheorghe and S. Hau, *Opt. Mater,* 2010, **32**, 1333–1336. https://doi.org/10.1016/j.optmat.2010.04.017.

32   X. Li, J. Zhu, Z. Man, Y. Ao, H. Chen, *Sci. Rep,* 2014, **4**, 4446. https://doi.org/10.1038/srep04446.

33   S. Karthi, G. S. Kumar, G. A. Kumar, D. K. Sardar, C. Santhosh and E. K. Girija, *J. Alloys Compd.*, 2016, **689**, 525–532. https://doi.org/10.1016/j.jallcom.2016.08.005.

34   Y. Xie, W. He, F. Li, T. S. H. Perera, L. Gan, Y. Han, X. Wang, S. Li and H. Dai, *ACS Appl. Mater. Interfaces*, 2016, **8**, 10212–10219. https://doi.org/10.1021/acsami.6b01814.

35   I. A. Neacsu, A. E. Stoica, B. S. Vasile and E. Andronescu, *Nanomaterials.* 2019, **9**, 239,

https://doi.org/10.3390/nano902023936.

36   Z. Li, Y. Zhang, L. Huang, Y. Yang, Y. Zhao, G. El-banna and G. Han, *Theranostics*. 2016, **6,** 2380. https://doi.org/10.7150/thno.15914.

37   G. A. Kumar, C. W. Chen and R. E. Riman, *Appl. Phys. Lett,* 2007, **90**, 093123. https://doi.org/10.1063/1.2392284.

38   Z. Sun, M. Bingchu, Li. Weiwei, L. Zuodong, Su. Liangbi, J Am Ceram Soc. 2016, **99**, 4039-4044. https://doi.org/10.1111/jace.14463.

39   B. Xu, H. He, Z. Gu, S. Jin and T. Zhai, *J. Phys. Chem C,* 2017, **212**, 18280-18287. https://doi.org/10.1021/acs.jpcc.7b05639.

40   G. D. Jones and R. J. Reeves, *J. Lumin,* 2000, **87**. 1108-1111. https://doi.org/10.1016/S0022-2313(99)00559-1.

41   P. Cortelletti, P. Marco, B. Federico, P. Sonia, C.Paolo, C. Patrizia, V. Fiorenzo, S. Adolfo, *Cryst. Growth Des*. 2018, **8** 686-694. https://doi.org/10.1021/acs.cgd.7b01050.

42   D. Karthickraja, S. Karthi, G. A. Kumar, D. K. Sardar, G. C. Dannangoda, K. S. Martirosyan and E. K. Girija, *New J Chem.*, 2019, **43**, 13584–13593. https://doi.org/10.1039/c9nj02310c.

43   L. C. Mimun, G. Ajithkumar, C. Rightsell, B. W. Langloss, M. J. Therien and D. K. Sardar, *J. Alloys Compd.*, 2017, **695**, 280–285. https://doi.org/10.1016/j.jallcom.2016.10.202.

44   Z. Ovanesyan, L. C. Mimun, G. A. Kumar, B. G. Yust, C. Dannangoda, K. S. Martirosyan and D. K. Sardar, *ACS Appl. Mater. Interfaces*, 2015, **7**, 21465–21471. https://doi.org/10.1021/acsami.5b06491.

45   F. H. L. Starsich, P. Gschwend, A. Sergeyev, R. Grange and S. E. Pratsinis, *Chem. Mater.*, 2017, **29**, 8158–8166. https://doi.org/10.1021/acs.chemmater.7b02170.

46   R. A. Talewar, S. Mahamuda, K. Swapna and A. S. Rao, *J. Alloys Compd.*, 2019, **771**, 980–986. https://doi.org/10.1016/j.jallcom.2018.08.270.

47   V. Petit, P. Camy, J-L. Doualan, R. Moncorgé, *Appl Phys Lett.* 2006, **8**, 051111.

https://doi.org/10.1063/1.2169887.

48   K. Jaroszewski, M. Chrunik, P. G, A. Majchrowski and D. Kasprowicz, *J. Lumin,* 2018, **203**, 663-669. https://doi.org/10.1016/j.jlumin.2018.07.014

49   K. Li and R. Van Deun, *ACS Sustain. Chem. Eng.* 2019, **7**, 16284−16294. https://doi.org/10.1021/acssuschemeng.9b03308

50   K. Li and R. Van Deun, *J. Mater. Chem. C*, 2018, **6**, 7302–7310. https://doi.org/10.1039/c8tc02019a.

51   M. Rathaiah, L.G. Antonio Diego, B. Palamandala, K.J. Chancheemalapalli, L. Víctor, V. Vemula, *RSC Adv*, 2016, **6**, 78669-78677. https://doi.org/10.1039/C6RA13729F.

52   D. L. Dexter, *J. Chem. Phys.*, 1953, **21**, 836–850. https://doi.org/10.1063/1.1699044.

53   Förster, T, *Annalen der Physik.* 1948, **437***, 55–75. https://doi.org/10.1002/andp.19484370105.

54   F. Rivera-López, P. Babu, C. Basavapoornima, C.K. Jayasankar, V. Lavín, *J. Appl. Phys,* 2011, **109**, 123514. https://doi.org/10.1063/1.3580475.

55   K. Li and R. Van Deun, *Mater. Chem. Front.*, 2019, **3**, 403–413. https://doi.org/10.1039/c8qm00603b

56   Http://Www.Iso.Org/Iso/Home.Html.

CRediT authorship contribution statement

D. Karthickraja - Conceptualization, Data curation, Methodology, writing original draft, Writing - review & editing

G.A. Kumar – Conducted emission, Decay time and In-vitro depth penetration measurement, Visualization, Validation and review & editing

D.K. Sardar – Visualization, Validation and Discussion of results

S. Karthi – Data analysis and Roles/Writing

G.C. Dannangoda - Visualization and Validation

K.S. Martirosyan - Visualization and Validation

M. Prasath – Conducted MTT assay

M. Gowri - Conducted MTT assay and Discussion of results

E.K. Girija - Conceptualization, Data curation, Methodology, original draft, Supervision, Validation, Writing - review & editing

Declaration of interests

☒ The authors declare that they have no known competing financial interests or personal relationships that could have appeared to influence the work reported in this paper.

☐The authors declare the following financial interests/personal relationships which may be considered as potential competing interests:

The authors declare that they have no known competing financial interests or personal relationships that could have appeared to influence the work reported in this paper.

Highlights

➢ We have successfully prepared the $Nd^{3+} \rightarrow Yb^{3+}$ energy transfer system.

➢ Defects in CaF_2:Nd^{3+}/Yb^{3+} lattice are repaired with Na^+ ion co-doping

➢ The optical property of luminescent particles have been tuned *via* co-doping of Na^+ and heat treatment process.

➢ *Ex vivo* optical imaging experiment confirms the feasibility of deep tissue imaging